

# Flash droughts exacerbate global vegetation loss and delay recovery

Received: 22 November 2024

Accepted: 24 November 2025

Published online: 08 December 2025

 Check for updates

Yuanfang Chai<sup>1,2</sup>, Chiyuan Miao<sup>1</sup>✉, Amir AghaKouchak<sup>3</sup>, Yadu Pokhrel<sup>4</sup>, Yongshuo Fu<sup>5</sup>, Xiaoyan Li<sup>1</sup>, Jiachen Ji<sup>1</sup>, Qi Zhang<sup>1</sup> & Josep Peñuelas<sup>6,7</sup>

The increasing incidence of flash droughts globally presents a great challenge to the agriculture sector, ecosystem resilience and water resource systems. Here we introduce a methodology that improves the accuracy of quantifying drought-induced global vegetation loss (using Normalized Difference Vegetation Index (NDVI)-derived metric). Our results reveal that NDVI loss during flash droughts (9.0%) is approximately 1.5 times higher than that during conventional droughts (5.3%), highlighting the increasing role of flash droughts as the key driver of drought-induced NDVI loss worldwide. Furthermore, we identify a significant upward trend (1.8% per decade) in global NDVI loss due to flash droughts, primarily driven by the increasing frequency of such events, which account for 81.2% of the overall trend. Although NDVI typically recovers within 36 pentads across more than  $9256.3 \times 10^4$  km<sup>2</sup> of the global land surface after flash droughts, there is a notable increase (0.4 pentads per year) in NDVI recovery time from 1982 to 2020, particularly in tropical rainforests and temperate forests. These findings highlight the alarming ecological consequences of increasingly frequent and intense flash droughts, with impacts expected to intensify in the future.

Rising global temperatures have intensified atmospheric aridity, with vapor pressure deficit (VPD) increasing by 5% in many regions since 1980s<sup>1,2</sup>. This amplifies evapotranspiration (ET), depleting soil moisture<sup>3,4</sup>. Concurrently, shifting precipitation patterns have reduced the frequency of light-to-moderate rainfall events while increasing the intensity of extreme precipitation, leaving longer dry intervals between rainfall events<sup>5-7</sup>. Additionally, declining snowpack and reduced snowmelt runoff further limit moisture recharge in regions dependent on seasonal snowmelt<sup>8-10</sup>. The combined drivers have accelerated the declining trend of global soil moisture, particularly in regions such as eastern China, Mongolia, southern Russia, the eastern European Plain, north-central Africa, the United States, and eastern Brazil, leading to an expansion of the soil drying area<sup>11</sup>. Soil droughts pose a great threat to global ecosystems<sup>12-15</sup>, and they can be broadly classified into one of two

types based on the speed of occurrence: flash drought<sup>16</sup> and conventional drought<sup>17</sup>. Flash drought manifests as a rapid decrease in soil moisture due to the combined effects of unusually high temperatures and extreme precipitation deficits, while conventional drought refers to a gradual and steady decline in soil moisture over an extended period<sup>16-21</sup>. Recent research indicates that there was a transition toward more flash droughts over 74% of global land area from 1951 to 2014<sup>17</sup>. This substantial increase in flash droughts poses unique challenges to vegetation<sup>17</sup>, as abrupt and severe drought may impede plants' ability to promptly adjust their physiological and ecological traits, leading to extensive damage or even complete loss of vegetation in affected regions<sup>17</sup>. As vegetation plays a critical role in regulating carbon, energy, and terrestrial water availability<sup>22-24</sup>, it is necessary to comprehensively analyze the ecological impacts of global flash droughts.

<sup>1</sup>State Key Laboratory of Earth Surface Processes and Disaster Risk Reduction, Faculty of Geographical Science, Beijing Normal University, Beijing, China.

<sup>2</sup>College of Geography and Environmental Sciences, Zhejiang Normal University, Jinhua, China. <sup>3</sup>Department of Civil and Environmental Engineering, University of California, Irvine, CA, USA. <sup>4</sup>Department of Civil and Environmental Engineering, Michigan State University, East Lansing, MI, USA. <sup>5</sup>College of Water Sciences, Beijing Normal University, Beijing, China. <sup>6</sup>CSIC, Global Ecology Unit CREAM-CSIC-UAB, Bellaterra, Catalonia, Spain. <sup>7</sup>CREAF, Center for Ecological Research and Forestry Application, Cerdanyola del Vallès, Catalonia, Spain. ✉e-mail: [miaocy@bnu.edu.cn](mailto:miaocy@bnu.edu.cn)

In recent years, several studies have been devoted to investigating and analyzing the profound effects of long-term drought on vegetation<sup>25,26</sup>. It has been well established that long-term atmospheric moisture deficit leads to a gradual depletion of soil moisture<sup>12</sup>, thereby severely constraining plant growth and development<sup>27–38</sup>. At the organismal scale, physiological threshold studies demonstrate that hydraulic dysfunction<sup>39</sup> and phloem transport collapse<sup>40</sup> jointly determine mortality risks. At the ecosystem scale, drought impacts on vegetation unfold across different spatial and temporal scales, including: (1) physiological and morphological changes such as reduced leaf area and partial canopy mortality<sup>41</sup>; (2) increased tree mortality rates across forest ecosystems<sup>42,43</sup>; and (3) large-scale die-off events<sup>44–47</sup>. At the global scale, recent observational and model-based studies indicate that soil moisture deficits have reduced global gross primary productivity (GPP) by an average of 15% during 1982–2016<sup>48</sup>. Looking ahead, future droughts are projected to decrease annual GPP, with global reductions expected to increase from 2.8 Pg C per year during 1850–1999 to between 4.5 and 4.7 Pg C per year during 2075–2099<sup>14</sup>. These findings reflect a continuum of drought severity, ranging from substantial physiological stress to ecosystem-scale collapse. The duration of vegetation recovery following long-term drought is also a topic of great importance to the health and stability of ecosystems, and it has become a prominent research focus in recent years<sup>49–53</sup>.

However, despite the significant advances made in understanding the consequences of long-term drought, limited attention has been paid to comprehensively investigating the implications of flash drought for vegetation<sup>54</sup>, especially at a global scale. Most studies have focused primarily on examining the effects of individual flash drought events on vegetation or have been limited to specific local regions, including the 2012 and 2015 central USA flash droughts<sup>18,55,56</sup> and the 2017 northern USA flash drought<sup>57</sup>. In particular, we still lack systematic, cross-scale analyses comparing the impacts of the two distinct drought types on vegetation dynamics. Furthermore, the extent to which vegetation can effectively recover following flash drought events, the associated recovery timelines, and how these recovery patterns differ from conventional drought responses need deeper investigation. Conventional approaches that neglect to account for the lagged response dynamics of vegetation and the compensatory effects between consecutive drought events may exhibit biases in quantifying the magnitude of drought-induced vegetation losses.

To address these knowledge gaps, we introduce an optimized method that incorporates factors previously overlooked in past studies. By leveraging satellite data and reanalysis datasets from NOAA and ERA5-Land, our study aims to comprehensively assess the impact of both flash and conventional droughts on global vegetation dynamics using NDVI-based metrics. We specifically focus on the dynamics of post-drought NDVI recovery during the growing seasons (April to September in the Northern Hemisphere and October to March in the Southern Hemisphere) over the period from 1982 to 2022. This approach will provide a deeper understanding of flash droughts and their effects, thereby supporting the development of targeted drought management strategies and helping to preserve essential ecosystem services in the context of climate change.

## Results and discussion

### Characteristics and drivers of global flash and conventional droughts

ERA5-land provides daily soil moisture data for three depth layers: Layer 1 (0–7 cm), Layer 2 (7–28 cm), and Layer 3 (28–100 cm)<sup>58</sup>. We integrated these layers to generate a top 1-meter composite soil moisture dataset. Daily values (0–100 cm) were then aggregated into pentad (5-day) means. To eliminate seasonal biases, pentad means were converted to percentiles by comparing each value against the 1982–2022 climatological distribution for the corresponding calendar

pentad. For instance, a soil moisture percentile of 40% indicates that the observed soil moisture was drier than 60% of historical values for that specific pentad.

Flash and conventional droughts were identified based on their distinct soil moisture trajectories (Fig. 1a). Briefly, flash droughts are characterized by a rapid intensification (a decline rate of  $\geq 5\%$  per pentad) from above the 40th to below the 20th soil moisture percentile. This 5% threshold has been extensively validated in previous studies as effectively distinguishing flash droughts from conventional drought events<sup>17,59–61</sup>. In contrast, conventional droughts exhibit a more gradual development, lacking this rapid intensification phase (Fig. 1b). Our independent validation confirms that this framework successfully identifies observed flash drought events (Supplementary Text 1 and Supplementary Fig. 1).

Figure 2a, b shows that the frequency of both flash and conventional droughts is highest in the mid-to-high latitudes of the Northern Hemisphere compared to other global regions. In this area, the occurrence of flash droughts clearly exceeds that of conventional droughts, especially between 30°N and 60°N. At the global scale, the average occurrence frequency is 0.37 events per year for flash droughts and 0.25 events per year for conventional droughts, with the former being approximately 1.5 times more frequent. Trend analysis indicates that the frequencies of both types have significantly increased, with rates of 0.034 events per decade (slope = 0.034 events per decade, 95% Confidence Intervals = [0.025, 0.044],  $t(df = 39) = 7.32$ , and  $p < 0.01$ ) for flash droughts and 0.015 events per decade (slope = 0.015 events per decade, 95% Confidence Intervals = [0.009, 0.022],  $t(df = 39) = 4.93$ , and  $p < 0.01$ ) for conventional droughts (Fig. 2c); notably, the increase in flash droughts is more than double that of conventional droughts.

Drought intensity is characterized by the minimum soil moisture percentile during drought periods, representing the lowest position in the historical climatological distribution (0–100%, where 0% is the driest and 100% the wettest). Figure 2d, e shows that drought intensity is most pronounced in tropical rainforest regions, likely due to high water demand from dense NDVI, which amplifies drought through elevated transpiration. This suggests that drought severity in these regions is driven not only by climatic factors like high temperatures and precipitation deficits but also by local NDVI effects. During flash droughts, the global average minimum soil moisture percentile is 5.6% (Fig. 2d, indicating soil moisture dropped to levels drier than 94.4% of all historical values), roughly half that during conventional droughts (11.9%, Fig. 2e), indicating that flash droughts are considerably more intense. Trend analysis reveals decreasing minimum soil moisture percentile over time for both flash ( $-0.08\%$  per decade) and conventional droughts ( $-0.09\%$  per decade), implying increasing drought severity (Fig. 2f).

Drought duration (corresponding to the gray shaded area in Fig. 1) shows shorter durations in tropical rainforest biomes for both drought types, reflecting seasonal precipitation patterns typical of tropical regions. On average, flash droughts last 8.3 pentads (Fig. 2g), about 0.8 pentads shorter than conventional droughts (Fig. 2h). Trends indicate increasing durations over time for both flash (0.034 pentads per decade) and conventional droughts (0.102 pentads per decade) (Fig. 2i).

Using multiple linear regression, we identified the key drivers of soil moisture depletion (Supplementary Texts 2, 3). Precipitation deficit emerged as the primary driver for both flash droughts ( $74.3\% \pm 17.9\%$ ) and conventional droughts ( $73.7\% \pm 14.6\%$ ). In contrast, evapotranspiration and snowmelt were secondary contributors, albeit with substantial regional influence (Supplementary Text 2 and Supplementary Figs. 2–10).

Furthermore, our improved maximum correlation approach reveals a faster hydrological response to precipitation deficits for flash droughts (average 3.4-pentad lag) than for conventional droughts (3.8-

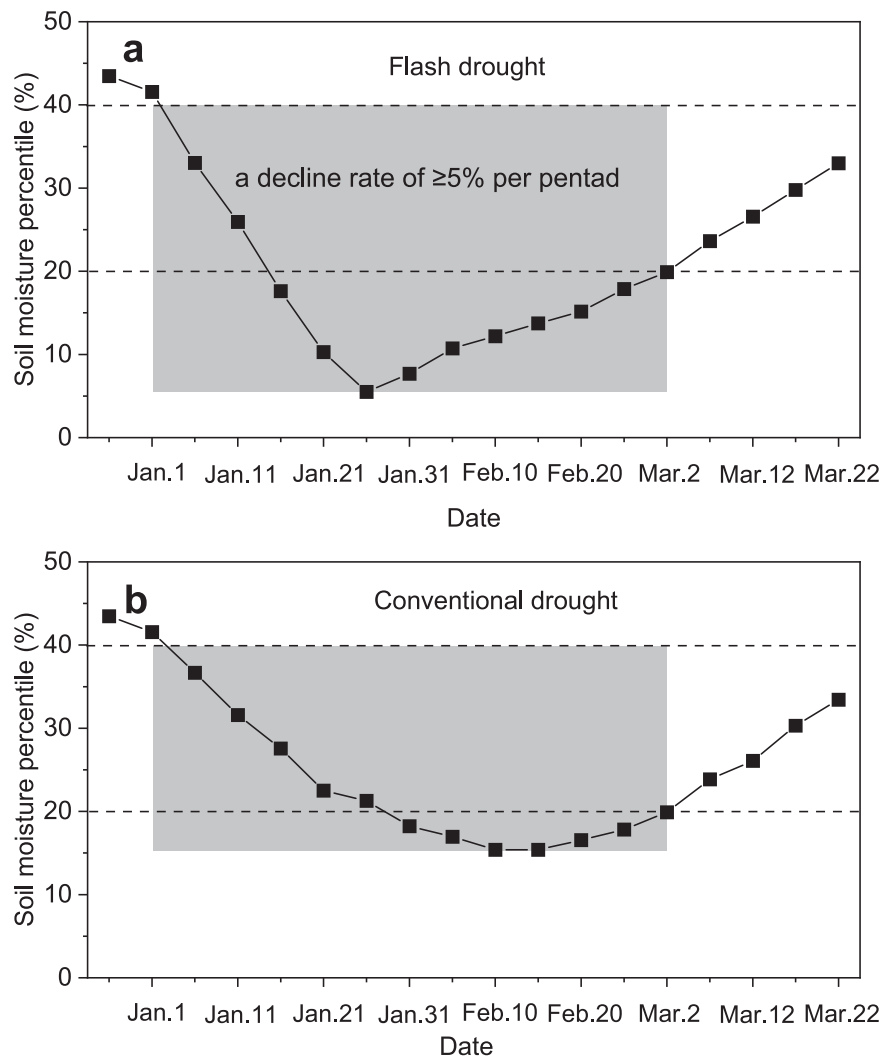


**Fig. 1 | Schematic representation of soil moisture trajectories and definition criteria for flash versus conventional droughts.** **a** Flash drought trajectory. The event is identified using the following criteria<sup>17</sup>: (1) Soil moisture percentile drops from above the 40th percentile to below the 20th percentile. (2) The average rate of decline during this intensification phase must be at least 5% per pentad. (3) The onset concludes when soil moisture falls below the 20th percentile and the rapid

decline ceases. (4) The event terminates when soil moisture recovers above the 20th percentile. (5) The entire event must persist for at least 4 pentads.

**b** Conventional drought trajectory. Conventional droughts are defined as sub-seasonal drought events that do not meet the rapid intensification criterion of flash droughts (i.e., the rate of decline is  $< 5\%$  per pentad). The gray shaded areas represent the periods when drought conditions occur.

pentad lag). This response is particularly accelerated in arid regions (as short as 2.4–2.8 pentads), where limited soil moisture buffering capacity curtails the system’s ability to mitigate water scarcity (Supplementary Text 2).

### Spatial and temporal patterns of NDVI vulnerability to droughts

To systematically assess drought impacts on NDVI, we have incorporated several advancements to enhance the robustness and comprehensiveness of our approach in analyzing daily NDVI data from the NOAA Climate Data Record (1982–2022).

During the initial stages of drought (Fig. 3a), NDVI undergoes a phase called the drought tolerance period, during which NDVI can withstand reduced water availability through physiological and biochemical adaptations while maintaining normal growth and development<sup>62</sup>. During this period, the observed NDVI values in Fig. 3a fluctuate up and down in the green range, without showing a continuous decrease. In our analysis of drought impacts on NDVI, this period was excluded. In contrast, even after the drought ends, there is a subsequent period during which NDVI continues to decline, known as the lag response period (Fig. 3a)<sup>63,64</sup>. It is characterized by a lack of

immediate recovery or fast growth in NDVI, despite the availability of water resources. This delayed response is attributed to the persistent impact of the drought on the physiological and ecological processes of NDVI. However, traditional methods have typically quantified drought-induced NDVI losses by directly relating observed NDVI anomalies to the duration of drought events. While this provides a valuable baseline, it may underestimate the full extent of NDVI impacts by not accounting for the reduction in NDVI that persists during the lag response period. In our analysis, we incorporated the lagged effects of drought on NDVI dynamics, providing a more comprehensive assessment of drought impacts. Our comparative analysis reveals that traditional methods neglecting NDVI lag effects underestimate drought-induced NDVI losses by 16.0% (flash droughts, Supplementary Fig. 11a) and 30.9% (conventional droughts), affecting  $9720.4 \times 10^4 \text{ km}^2$  and  $10197.4 \times 10^4 \text{ km}^2$  of global land area respectively (Supplementary Fig. 11b,c). These systematic underestimations underscore the importance of considering persistent effects on NDVI that extend beyond the immediate drought period.

During the recovery period between two drought events, NDVI may not fully return to its pre-drought state, remaining in a semi-

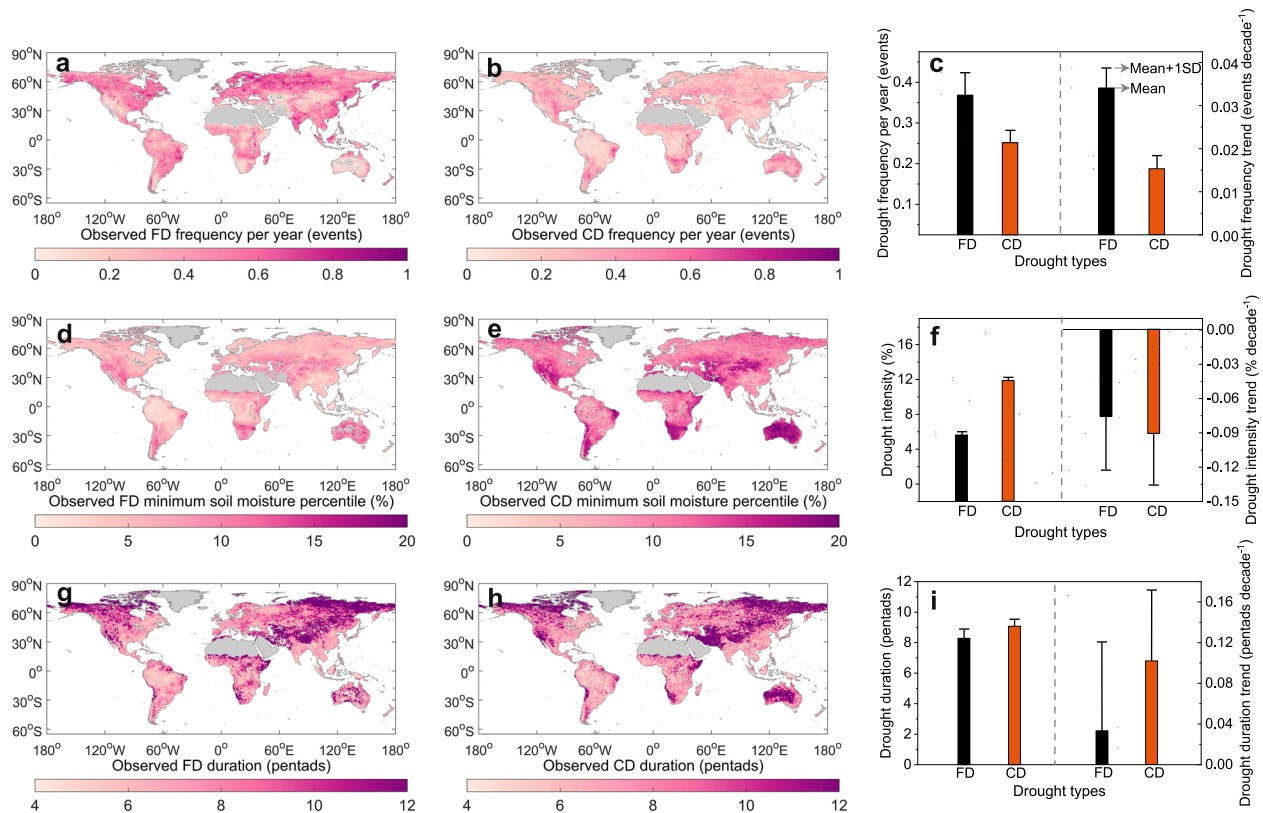


**Fig. 2 | Global comparison of drought frequency, intensity, and duration (1982–2022).** **a, b** depict the multi-year average frequencies of flash droughts (FD) and conventional droughts (CD), respectively. **c** shows the global mean frequency and trends for both drought types. Data are presented as mean values  $\pm$  SD (standard deviation,  $n = 41$ , biological replicates). **d, e** present the multi-year average minimum soil moisture percentiles during flash and conventional droughts, respectively. The minimum soil moisture percentile reflects drought intensity.

**f** illustrates the global mean minimum soil moisture percentile during drought periods, along with trends. Lower values indicate higher drought severity. Data are presented as mean values  $\pm$  SD ( $n = 41$ , biological replicates). **g, h** show the average durations of flash and conventional droughts (pentads). **i** displays the global mean durations and their trends. Data are presented as mean values  $\pm$  SD ( $n = 41$ , biological replicates).

recovered condition. As a result, a portion of the NDVI loss observed during the current drought should be attributed to the legacy effects of the previous drought, rather than the current event alone. Failure to isolate this offset effect can result in overestimation of the direct impacts of the current drought. Through comparative analysis, we found that neglecting the offset effects overestimated the global NDVI losses by up to 13.3% for flash drought and 16.1% for conventional drought (Supplementary Fig. 11d). This overestimation was observed across  $9191.8 \times 10^4 \text{ km}^2$  of the global land area for flash drought and  $8005.8 \times 10^4 \text{ km}^2$  for conventional drought (Supplementary Fig. 11e, f). Therefore, in quantifying the ecological consequences of drought, we accounted for this offset effect (See Methods).

Another methodological improvement is that we separated NDVI declines caused by fires from those driven solely by drought stress by overlaying the burned area data with our NDVI and drought datasets, masking affected pixels to ensure observed NDVI decline was drought-related (Supplementary Text 4 and Supplementary Fig. 12). In our analysis, we primarily focused on the time frame from the conclusion of the drought tolerance period to the end of the NDVI lag response period in order to assess the impact of a specific drought event on NDVI (i.e., yellow-shaded region in Fig. 3a, See Methods).

Using the above enhanced methodology, we estimate the impacts of flash droughts and conventional droughts on global NDVI for the period from 1982 to 2022. We find that the reduction in global average NDVI due to flash droughts was found to be 9.0%, whereas for conventional droughts it was 5.3% (Fig. 3b). Our geospatial analyses indicate the mid-to-high-latitude regions of the Northern Hemisphere

experienced the largest NDVI declines under both flash and conventional droughts, exceeding the global mean by 18.2% (Supplementary Fig. 13). Additionally, Fig. 3c shows that over  $8276.5 \times 10^4 \text{ km}^2$  of the global land area experienced a greater decrease in NDVI due to flash droughts compared with conventional droughts. This is further confirmed by comparing NDVI losses between flash and conventional droughts under identical frequency scenarios (i.e., with equal drought occurrence rates for both types). We find that NDVI losses during flash droughts consistently exceeded those during conventional droughts in every year analyzed (mean difference: +27.8% globally, Supplementary Fig. 14). Consequently, these sudden and intense flash drought events have become the key factor in global NDVI reduction.

Importantly, we found statistically significant increasing trends in global NDVI loss caused by both flash drought (slope = 0.0033 per decade, 95% Confidence Intervals = [0.0027, 0.0039],  $t(df = 39) = 10.8$ , and  $p < 0.01$ ) and conventional drought (slope = 0.0016 per decade, 95% Confidence Intervals = [0.0012, 0.0020],  $t(df = 39) = 8.8$ , and  $p < 0.01$ ) from 1982 to 2022 (Fig. 3b). The annual rates of increase are 1.8% of the global mean NDVI level per decade for flash drought and 0.9% of NDVI per decade for conventional drought. These results demonstrate a progressive exacerbation of the adverse impacts of drought on NDVI, with flash drought exhibiting approximately a two-fold higher acceleration in NDVI loss compared to conventional drought. Furthermore, the analyses reveal that the increased NDVI losses induced by drought from the 1982–2001 period to the 2002–2022 period were spatially extensive, encompassing  $8121.8 \times 10^4 \text{ km}^2$  of global land areas for flash drought (Fig. 3d) impacts and  $7180.7 \times 10^4 \text{ km}^2$  for conventional drought impacts (Fig. 3e).

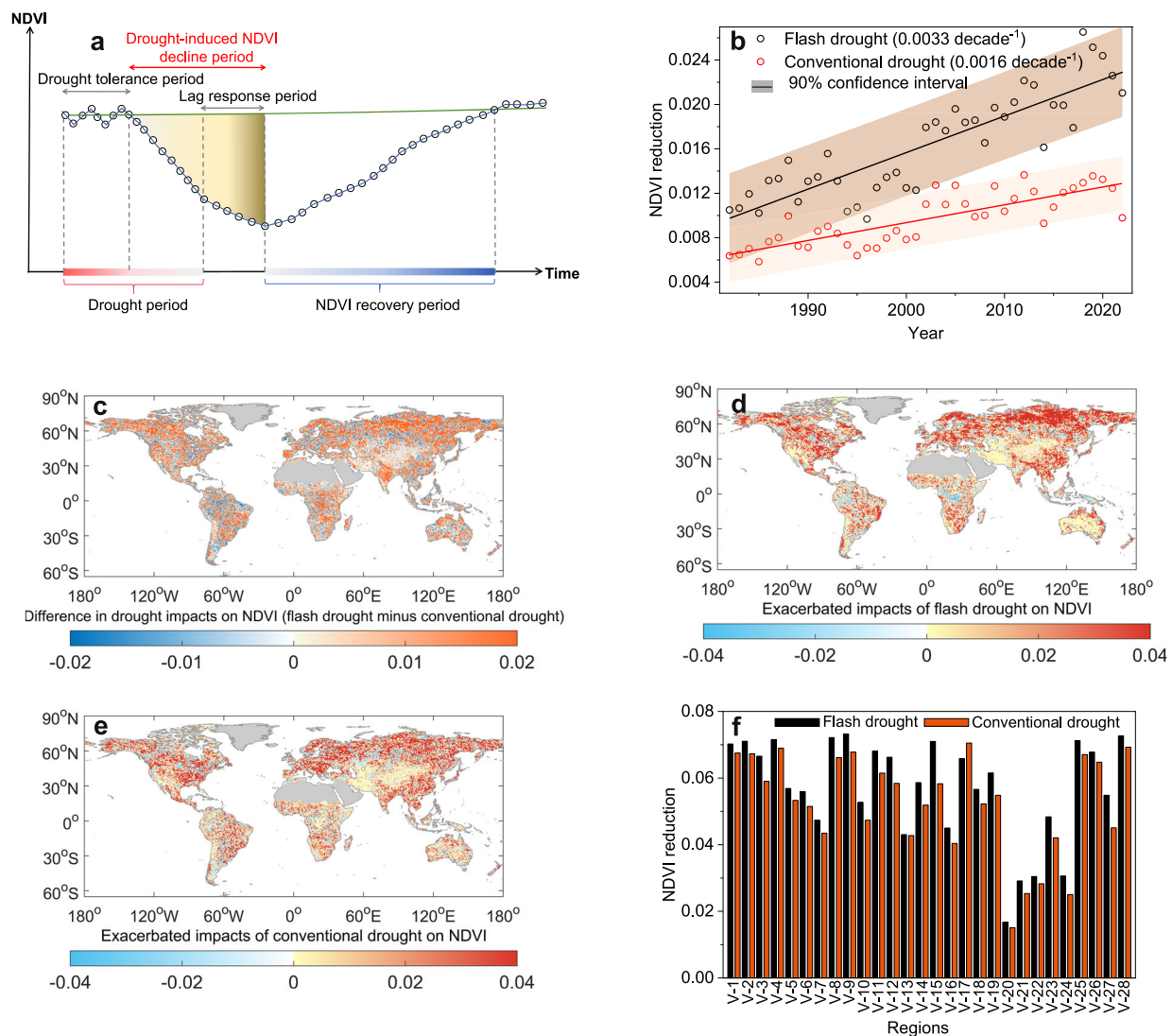


**Fig. 3 | Characteristics of global NDVI losses in response to flash and conventional droughts during the vegetation growing season for the period of 1982–2022.** **a** is the conceptual diagram illustrating the impact of a specific drought event on NDVI. The green curve represents the expected NDVI trajectory in the absence of drought, modelled using a smooth spline regression (See Method). The blue line represents the observed NDVI trajectory under drought conditions. Vegetation is considered fully recovered once NDVI returns to its pre-drought level. **b** shows the trend in the reduction of global average values that are attributable to flash drought (black) or conventional drought (red). Data in Fig. 3b are presented as the mean (solid line) with a shaded 90% prediction band, representing the range within which future observations are expected to fall with 90% probability.

**c** presents the difference in multi-year average NDVI reduction between flash-drought-induced and conventional-drought-induced impacts (flash drought minus conventional drought). **d** depicts the difference calculated by subtracting the values of NDVI reduction due to flash drought between the period 2002–2022 and the period 1982–2001. Like **d**, **e** depicts conventional drought. **f** shows the multi-year average reduction in NDVI values observed under the impact of drought across 28 regions (1982–2022), each with a single dominant vegetation type. The classification of different vegetation types is based on the land cover classification from the European Space Agency (ESA) Climate Change Initiative (CCI) Land Cover dataset.

We analyzed the response characteristics of 28 regions (each with a single dominant vegetation type) to flash drought and conventional drought (Supplementary Figs. 15–17). During the early growing season, all regions exhibit characteristic seasonal NDVI increases under normal (pre-drought) conditions, reflecting typical phenological development (Supplementary Figs. 15–17). However, divergent response mechanisms become evident during drought events. The results show that the drought tolerance period (during which NDVI remains stable despite water stress) lasts only 1–2 pentads for flash droughts, followed by a sharp NDVI decline, whereas it extends to 3–4 pentads for conventional droughts. This suggests that rapid soil moisture depletion during flash droughts shortens the window for physiological adjustments, while the gradual drying of conventional droughts allows NDVI to sustain tolerance mechanisms longer.

Across all the vegetation types studied, the impact of flash drought was found to be greater than the impact of conventional drought (Fig. 3f). We find that closed (V-9) and closed-to-open (V-8) deciduous broadleaved forests, along with closed-to-open evergreen (V-11) and deciduous (V-15) needleleaved forests, exhibit greater vulnerability to both flash and slow-onset drought events compared to other vegetation functional types. These forest ecosystems are predominantly distributed across mid-to-high latitudes in the Northern Hemisphere, regions historically characterized by pronounced drought intensity, frequency, and duration. Beyond forests, herbaceous systems—including crops, grasslands, and shrublands—also exhibit strong sensitivity to flash drought events. Notably, croplands are particularly susceptible to rapid-onset drought stress, with impact severity increasing over time. This pattern raises urgent concerns

regarding cascading risks to food security, agricultural economies, and livelihoods dependent on rainfed and irrigated crop production. In contrast, tropical evergreen broadleaf forests demonstrate remarkable resilience to flash droughts, showing only 83% of the NDVI reduction observed in other vegetation types, despite experiencing drought conditions that are 18% more intense than the global average. This unexpected resistance may result from three synergistic factors: (1) shorter drought durations (14.6% below the global mean), (2) deep-rooted water access—Amazonian roots extend beyond 150 cm—coupled with substantial groundwater reserves<sup>65–67</sup>, and (3) frequent high-intensity precipitation events that rapidly recharge soil moisture. These adaptive traits collectively buffer tropical rainforests against rapid soil moisture depletion, even under heightened drought stress.

We conducted additional analyses by calculating the ratio of NDVI decline rate to soil moisture decline rate (termed the sensitivity ratio) specifically in regions with the same drought frequencies. As shown in Supplementary Fig. 18, the sensitivity ratio value during flash drought periods ( $0.0034 \pm 0.0007\%^{-1}$ ) is higher than during conventional drought periods ( $0.0018 \pm 0.0003\%^{-1}$ ) across all the vegetation types. These results highlight fundamental differences in affecting NDVI between flash drought and conventional drought.

To further analyze the differential response characteristics of NDVI to the two types of drought, we calculated the incremental NDVI losses corresponding to each 1% increase in the soil moisture percentile decline rate (from 1% to 10% per pentad). The results reveal that NDVI maintains relatively effective physiological regulation to mitigate water stress when soil moisture decline rates are below 5% per pentad (conventional drought), with NDVI loss increasing at a gradual, near-linear rate (orange histogram in Supplementary Fig. 19). However, when the decline rate exceeds 5% per pentad (flash drought), water stress may exceed critical physiological thresholds, triggering an acceleration in NDVI loss. The incremental NDVI losses nearly double compared to those below 5% per pentad, showing a jump in NDVI response (black histogram in Supplementary Fig. 19). This analysis also indicates that 5% per pentad may represent a meaningful ecological threshold where NDVI shifts from gradual degradation to accelerated damage accumulation.

### Mechanisms underlying drought impacts on NDVI

Figure 3b shows that flash droughts caused greater NDVI losses (9.0%) compared to conventional droughts (5.3%) during 1982–2022. Using spatial multiple linear regression analysis (see Method), we quantified the relative contributions of four drought characteristics—soil moisture decline rate, drought frequency, drought intensity, and drought duration—to NDVI losses. The analysis indicates that drought frequency (41.8%) and soil moisture decline rate (40.2%) are the dominant factors explaining the greater NDVI losses associated with flash droughts. Conversely, drought intensity (10.9%) and duration (7.1%) played smaller roles. The higher contribution of drought frequency reflects the more frequent occurrence of flash droughts—averaging 0.37 events per year compared to 0.25 for conventional droughts—leading to accumulated NDVI losses over time. Meanwhile, the rapid soil moisture decline in flash droughts may impose immediate water stress, triggering stomatal closure that restricts photosynthesis and increasing the risk of xylem embolism, which can cause swift NDVI decline. In contrast, the gradual moisture depletion characteristic of conventional droughts allows NDVI to activate adaptive strategies—such as dynamic stomatal regulation and increased deep-root water uptake—thereby mitigating NDVI losses.

Using a temporal multiple regression analysis, we examined the dominant factors contributing to the increasing drought-induced global NDVI loss from 1982 to 2022. As shown in Supplementary Table 3, the results indicate that the trend of significantly increasing drought frequency (slope = 0.034 events per decade, 95% Confidence Intervals = [0.025, 0.044],  $t(df = 39) = 7.32$ , and  $p < 0.01$ ,

Supplementary Fig. 20) is the dominant factor underlying the increasing flash-drought-induced NDVI loss during this period, accounting for 81.2% of the observed change. In contrast, the slightly increasing soil moisture decline rate ( $0.14\% \text{ pentad}^{-1}$  per decade), increasing drought duration (0.034 pentads per decade) and the increasing drought intensity ( $0.08\% \text{ per decade}$ ) play secondary roles, contributing 3.9%, 4.8% and 10.1%, respectively. A similar pattern was found for conventional drought (Supplementary Table 3): increasing frequency (0.015 events per decade, Supplementary Fig. 20) explained 79.1% of the NDVI loss trend, followed by drought intensity (17.3%), soil moisture decline rate (3.5%) and drought duration (0.1%).

We extended this trend analysis across vegetation types (Supplementary Fig. 21). The results indicate that the rising drought frequency remained the dominant factor intensifying NDVI losses across all vegetation types. However, in irrigated croplands, both drought intensity and the soil moisture decline rate also played substantial roles, each explaining over 10% to the increasing trend in NDVI losses under both flash and conventional droughts.

### Global patterns of NDVI drought recovery

After the NDVI lag response period (Fig. 3a), the NDVI enters the recovery period. The period is defined as the time when NDVI begins to recover and reestablish its normal growth and developmental state until it reaches the normal level without the impact of drought for the corresponding period. The duration of this phase corresponds to the NDVI recovery time. The spatial and temporal patterns of global NDVI recovery time following drought events is of crucial importance for ecological restoration planning, natural resource management, climate change adaptation, and ecosystem services assessment<sup>68,69</sup>. Our analysis estimates that the average global duration required for NDVI to recover to pre-drought levels after flash drought events is  $31 \pm 6.8$  pentads for the period from 1982 to 2022 (Supplementary Fig. 22a). In contrast, the average recovery time after conventional drought events is estimated to be  $27.8 \pm 6.6$  pentads (Supplementary Fig. 22b). Moreover, across  $7309.6 \times 10^4 \text{ km}^2$  of terrestrial regions globally, especially mid-to-high latitude areas in the Northern Hemisphere and tropical regions, the NDVI recovery time following flash drought events exceeds that of conventional drought events (Fig. 4a), with a global average difference of 3.2 pentads. These findings highlight the distinct impacts of flash and conventional droughts on NDVI recovery time.

Figure 4b shows that NDVI can typically recover to normal levels within 36 pentads—across  $9256.3 \times 10^4 \text{ km}^2$  of the global land area for flash drought and  $9991.1 \times 10^4 \text{ km}^2$  for conventional drought. Furthermore, within 54 pentads, a very high proportion of NDVI—irrespective of drought type—exhibits signs of recovery, encompassing around  $11602.6 \times 10^4 \text{ km}^2$  of the global land area. These findings suggest that, in most scenarios, the restoration of NDVI to pre-drought levels occurs within a time frame ranging from 36 to 72 pentads. Here we further examine the impact of extreme and long-term drought events—defined as droughts with durations at or above the 90th percentile of all drought events—on NDVI recovery (Supplementary Text 5). We found that approximately  $87.5 \times 10^4 \text{ km}^2$  and  $39.9 \times 10^4 \text{ km}^2$  of areas have still not recovered to pre-drought NDVI levels after experiencing prolonged flash and conventional droughts (Supplementary Fig. 25), respectively.

We analyzed the trend in global average values from 1982 to 2020 for NDVI recovery time after drought events (Supplementary Fig. 22c, d). The results show a significant increasing trend (slope = 0.4 pentads, 95% Confidence Intervals = [0.29, 0.57],  $t(df = 37) = 6.2$ , and  $p < 0.01$ ) in the global average NDVI recovery time during the period of 1982–2020, with an annual increase of 0.4 pentads for both flash drought and conventional drought (Supplementary Fig. 22c, d). This increasing trend was observed over  $8225.0 \times 10^4 \text{ km}^2$  of the global land surface for flash drought (Supplementary Fig. 22e) and

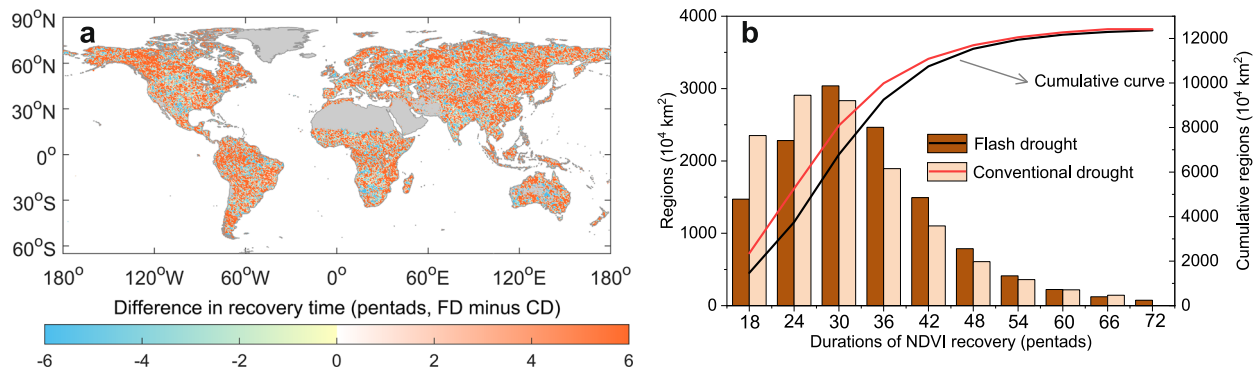


**Fig. 4 | Global NDVI recovery time during the vegetation growing season for 1982–2022. a** presents the difference between the long-term average NDVI recovery time following flash drought (FD) events and the long-term average NDVI recovery time following conventional drought (CD) events (flash drought recovery

time minus conventional drought recovery time). **b** displays the land area in regions with different durations of NDVI recovery. The cumulative percentage curve shows the land area in regions with NDVI recovery time less than or equal to a certain value.

$8689.1 \times 10^4 \text{ km}^2$  for conventional drought (Supplementary Fig. 22f). This prolongation of NDVI recovery time has potential implications for reducing both ecosystem productivity and carbon sequestration capacity and thus exacerbating climate degradation.

Analysis conducted for different regions (each with a single dominant vegetation type, Supplementary Fig. 26) indicated that tropical rainforests and temperate forests exhibit longer recovery periods following drought events, particularly the evergreen broadleaved trees in the Amazon rainforest, which were estimated to require up to 36.2 pentads and 33.8 pentads for full recovery after flash drought and conventional drought, respectively. These findings are consistent with previous research findings<sup>68</sup>. In contrast, irrigated croplands (23.6–28.2 pentads), grasslands (25.8–27.2 pentads), and shrublands (26.0–28.6 pentads) display shorter recovery periods. Consistent with these values, recent evidence also reported that drought legacy effects on forests are more pronounced compared to shrubs and grasses<sup>63</sup>.

Our study provides a comprehensive global assessment of the escalating ecological threats posed by flash droughts. By refining methodologies to account for lagged responses and offset effects, we find that flash droughts induce greater NDVI losses than conventional droughts. This disparity is primarily attributed to their higher frequency (contributing 41.8%) and accelerated soil moisture decline rates (40.2%). We also document a significant upward trend in global NDVI loss due to flash droughts (slope = 0.0033 per decade, 95% Confidence Intervals = [0.0027, 0.0039],  $t(df = 39) = 10.8$ , and  $p < 0.01$ ), primarily driven by their rapidly increasing frequency. While NDVI typically recovers within half year over most land areas following flash droughts, the recovery time is longer than after conventional droughts (average difference of 3.2 pentads) and is exhibiting a prolongation trend of 0.4 pentads per year since 1982, particularly in critical biomes like tropical rainforests and temperate forests.

These findings underscore that the accelerating shift towards more frequent, intense, and rapid-onset flash droughts poses an ecological challenge, highlighting the vulnerability of NDVI to abrupt hydrological changes under a warming climate. The amplified NDVI loss and delayed recovery may threaten ecosystem productivity, carbon sequestration capacity, and critical services such as food security. Additionally, flash droughts exhibit a shorter tolerance period and more rapid NDVI decline, often requiring prompt measures such as emergency irrigation and water reallocation. In comparison, conventional droughts, with their extended adaptation window, generally permit more measured response strategies. From a management perspective, these differences suggest that flash droughts may benefit from dedicated rapid-response frameworks, while conventional droughts might be managed through more systematic approaches. In summary, addressing this challenge requires integrating the unique

characteristics of flash droughts into climate adaptation strategies, ecosystem management, and drought monitoring systems to mitigate their escalating ecological consequences.

## Methods

### Method for analysis of global NDVI vulnerability to drought

The NDVI data used in this study were obtained from the NOAA Climate Data Record (CDR) of the Advanced Very High Resolution Radiometer (AVHRR) Surface Reflectance, with a spatial resolution of  $0.05^\circ \times 0.05^\circ$  spatial resolution<sup>70</sup>. NDVI is a widely used proxy for vegetation greening dynamics, calculated based on the difference between near-infrared and red light reflectance. However, this index cannot resolve vertical vegetation structure or distinguish between plant species with similar reflectance characteristics, limiting its ability to represent community composition. To ensure NDVI changes primarily reflect drought stress rather than phenological cycles, we focused analysis on the vegetation growing season (the period coinciding with peak vegetation activity and monsoon rains). This avoids cold dormancy and dry-season leaf shedding effects. The growing season classification scheme employed in this study (April–September for the Northern Hemisphere and October–March for the Southern Hemisphere) aligns with mainstream approaches in global vegetation research<sup>17,71,72</sup>. It should be noted that this classification may not fully capture seasonal characteristics in certain special ecoregions, such as semi-arid areas with winter growing seasons and tropical regions with distinct seasonal variations. This important aspect warrants further refinement in future studies through the development of more region-specific growing season criteria.

We first fitted a smooth spline over the NDVI data for a specific pentad during the period from 1982 to 2022. If that pentad in a particular year was experiencing drought, the NDVI data for that year's pentad was excluded from the smoothing spline fitting process. Then, the spline was used to estimate the average NDVI for the specific pentad of interest. This average NDVI serves as a representation of the vegetation state in the absence of drought impact<sup>44</sup>. Given the observed NDVI value  $y_{i,k}$  in a specific pentad  $k$  at the  $i$ -th year ( $i = 1, 2, \dots, n$ ), the calculation of smoothing spline can be summarized as follows:

$$Q(f) = \sum_{i=1}^n (y_{i,k} - f(x_i))^2 + \gamma \int f''(x) dx \quad (1)$$

Where  $Q$  is the objective function of spline  $f(x)$ ;  $x_i$  represents the year that is sequentially ordered as the  $i$ -th year ( $x_i = 1982, 1983, \dots, 2022$ );  $\gamma$  is a smoothing parameter;  $f''(x)$  is the second derivative of the spline that represents the smoothness of the curve. For a given  $\gamma$  value, we can obtain the optimal smoothing function  $f(x)$  by minimizing the target function  $Q(f)$ .

Then, the deviation (or anomaly) between the observed NDVI (affected by drought,  $NDVI_{obs,k}$ ) and the estimated spline ( $NDVI_{spline,k}$ ) was used to quantify the drought-induced NDVI losses in a specific pentad  $k$  in the year  $x_i$  for a certain grid cell ( $NDVI_{loss,k}$ )<sup>14</sup>. Namely,

$$NDVI_{loss,k} = NDVI_{obs,k} - NDVI_{spline,k} \quad (2)$$

Taking Fig. 3a as an example, each data point represented by a circle on the blue line corresponds to the observed NDVI value for a specific pentad in a given year. Each pentad is associated with a spline curve, and the collection of these spline curves is shown as the green line in the graph, depicting the trend for NDVI variation throughout the year without drought impact. Therefore, during the period of drought impact on NDVI, from the end of the drought tolerance period to the end of the NDVI lag response period, the difference between the blue line and the green line represents the NDVI losses caused by the drought event (flash or conventional drought).

**Considering offset effects between consecutive drought events**

When the current drought occurred, the NDVI loss caused by the previous drought had still not recovered to the normal level, leaving a residual deficit ( $RD$ , Eq. 3). The total NDVI loss during the current drought was a certain amount ( $NDVI_{loss}$ , Eq. 4). Of this total loss, a portion should be attributed to the carryover effects of the previous drought and thus excluded from the impacts of the current drought. Therefore, the net NDVI loss directly attributable to the current drought ( $NDVI_{impact}$ ) can be calculated by subtracting the carryover effects from the total loss during the current drought event (Eq. 5).

$$RD = NDVI_{spline,k=1} - NDVI_{obs,k=1} \quad (3)$$

$$NDVI_{loss} = \sum_{k=1}^m (NDVI_{obs,k} - NDVI_{spline,k}) \quad (4)$$

$$NDVI_{impact} = NDVI_{loss} - RD \quad (5)$$

The current drought event lasted for  $m$  pentads, where  $k$  ( $k = 1, 2, \dots, m$ ) represents the  $k$ -th pentad of the current drought event.  $NDVI_{spline,k=1}$  and  $NDVI_{obs,k=1}$  are the NDVI values obtained from the smooth spline fitting and the observed NDVI value, respectively, both at the first pentad of the current drought event.  $NDVI_{spline,k}$  and  $NDVI_{obs,k}$  are the NDVI values obtained from the smooth spline fitting and the observed NDVI value, respectively, both at the  $k$ -th pentad of the current drought event.

**Method for estimating the drought-induced NDVI losses across different vegetation types**

The vegetation classification is identified based on the global land cover maps provided by the European Space Agency (ESA) Climate Change Initiative (CCI) Land Cover dataset<sup>73</sup>. The spatial distribution of each vegetation type has been continuously evolving from 1992 to 2022 according to the ESA CCI Land Cover dataset. In this study, we focus our analysis only on the response characteristics of that vegetation type within fixed, unchanging regions over this time period.

**Method for estimating contributions of driving factors to variations in drought-induced NDVI loss**

To quantify the relative contribution of each driving factor to the variation in the drought-induced NDVI loss, we employed a multiple linear regression analysis (Eq. 6).

$$y = b_1 \cdot x_1 + b_2 \cdot x_2 + b_3 \cdot x_3 + b_4 \cdot x_4 + b_0 \quad (6)$$

Here,  $y$  represents the drought-induced NDVI loss amount;  $x_1$ ,  $x_2$ ,  $x_3$  and  $x_4$  represent the soil moisture decline rate (% pentad<sup>-1</sup>), drought frequency (events), drought intensity (%), and drought duration (pentads), respectively;  $b_1$ ,  $b_2$ ,  $b_3$  and  $b_4$  are regression coefficients, and  $b_0$  is the residual error term. Regressions were estimated on the annual anomalies of the variables, an approach that could remove the effects of background levels while retaining the impacts of interannual variations on NDVI growth, thereby reflecting the sensitivities of NDVI growth to these factors<sup>74-76</sup>.

Based on the estimated regression coefficients, we can calculate the standardized coefficients of  $x_1$  ( $stc_1$ ),  $x_2$  ( $stc_2$ ),  $x_3$  ( $stc_3$ ) and  $x_4$  ( $stc_4$ ) using Eqs. 7-10, respectively.

$$stc_1 = b_1 \cdot \frac{std(x_1)}{std(y)} \quad (7)$$

$$stc_2 = b_2 \cdot \frac{std(x_2)}{std(y)} \quad (8)$$

$$stc_3 = b_3 \cdot \frac{std(x_3)}{std(y)} \quad (9)$$

$$stc_4 = b_4 \cdot \frac{std(x_4)}{std(y)} \quad (10)$$

Where  $std(x_1)$ ,  $std(x_2)$ ,  $std(x_3)$ ,  $std(x_4)$  and  $std(y)$  are the standard deviations of  $x_1$ ,  $x_2$ ,  $x_3$ ,  $x_4$  and  $y$ , respectively. The standardized coefficients provide a way to directly compare the relative importance of the different independent variables in the regression model. The magnitudes of the standardized coefficients indicate the relative importance of the corresponding independent variables in explaining the changes in drought-induced NDVI loss amount. Variables with larger standardized coefficients have a greater impact on the dependent variable.

Finally, using Eqs. 11-14, we can estimate the contribution rates of  $x_1$  ( $r_1$ ),  $x_2$  ( $r_2$ ),  $x_3$  ( $r_3$ ) and  $x_4$  ( $r_4$ ) to the variations in drought-induced NDVI loss amount from 1982 to 2022, based on the obtained standardized coefficients.

$$r_1 = \frac{stc_1}{(stc_1 + stc_2 + stc_3 + stc_4)} \quad (11)$$

$$r_2 = \frac{stc_2}{(stc_1 + stc_2 + stc_3 + stc_4)} \quad (12)$$

$$r_3 = \frac{stc_3}{(stc_1 + stc_2 + stc_3 + stc_4)} \quad (13)$$

$$r_4 = \frac{stc_4}{(stc_1 + stc_2 + stc_3 + stc_4)} \quad (14)$$

In this study, multiple linear regression analysis was conducted in two ways: spatial multiple regression analysis and temporal multiple regression analysis. Spatial multiple regression analysis was used to explain why the multi-year average flash drought-induced NDVI loss was greater than that of conventional drought-induced NDVI loss. Therefore, the dependent variable  $y$  was the difference between the multi-year average flash drought-induced NDVI loss and the conventional drought-induced NDVI loss across all grid cells. Similarly,  $x_1$ ,  $x_2$ ,  $x_3$  and  $x_4$  were also calculated as the differences between the corresponding flash drought and conventional drought metrics. Temporal multiple regression analysis was applied to investigate why flash (or conventional) drought-induced NDVI losses exhibited a significant

increasing trend from 1982 to 2022. Here,  $x_1$ ,  $x_2$ ,  $x_3$ ,  $x_4$  and  $y$  corresponded to time-series data.

### Reporting summary

Further information on research design is available in the Nature Portfolio Reporting Summary linked to this article.

### Data availability

Daily data on soil moisture (0–7 cm, 7–28 cm, and 28–100 cm), precipitation, ET and snowmelt were derived from the ERA5-land reanalysis dataset. The data were sourced from the Copernicus Climate Data Store at a  $0.25^\circ \times 0.25^\circ$  spatial resolution (<https://cds.climate.copernicus.eu/cdsapp#!/dataset/reanalysis-era5-land?tab=overview>)<sup>58</sup>. The daily global land temperature record was obtained from the Berkeley Earth land temperature dataset, which incorporates data from over 40,000 stations and employs kriging-based spatial interpolation at a  $1^\circ \times 1^\circ$  resolution, providing extensive spatial coverage from 1850 to the present (<https://berkeleyearth.org/data/>)<sup>77</sup>. Monthly precipitation and potential evapotranspiration data were derived from the HadCRUT4 dataset (hosted in the CEDA Archive). These data were interpolated using angular-distance weighting (ADW) from extensive weather station networks at a  $0.5^\circ \times 0.5^\circ$  resolution (<https://archive.ceda.ac.uk/>)<sup>78</sup>. The NDVI data used in this study were obtained from the NOAA Climate Data Record (CDR) of the Advanced Very High Resolution Radiometer (AVHRR) Surface Reflectance at a  $0.05^\circ \times 0.05^\circ$  spatial resolution (<https://www.ncei.noaa.gov/products/climate-data-records/normalized-difference-vegetation-index/>)<sup>70</sup>. Global land cover maps were obtained from the European Space Agency (ESA) Climate Change Initiative (CCI) Land Cover dataset. These maps provide 300-meter resolution data from 1992 to 2022, based on observations from the Project for On-Board Autonomy-Vegetation (PROBA-V), Sentinel-3 Ocean and Land Colour Instrument (OLCI), and Sentinel-3 Sea and Land Surface Temperature Radiometer (SLSTR) (<https://cds.climate.copernicus.eu/cdsapp#!/dataset/satellite-land-cover/>)<sup>79</sup>. The global burned area data were collected from the MODIS burned area product (available post-2000; <https://lpdaac.usgs.gov/products/mcd64a1v061/>)<sup>80</sup> and the AVHRR-LTDR burned area product (covering pre-2000; <https://catalogue.ceda.ac.uk/uuid/b1bd715112ca43ab948226d11d72b85e/>)<sup>81</sup>. We regridded all observational datasets to a common  $0.5^\circ \times 0.5^\circ$  latitude-longitude spatial resolution using bilinear interpolation.

### Code availability

The code for this study is available via Github at <https://github.com/Yuanchai1/Code-for-analyzing-drought-impacts-on-vegetation.git>.

### References

- Calvin, K. et al. IPCC, 2023: Climate Change 2023: Synthesis Report. Contribution of Working Groups I, II and III to the Sixth Assessment Report of the Intergovernmental Panel on Climate Change [Core Writing Team, H. Lee and J. Romero (Eds.)]. IPCC, Geneva, Switzerland.
- Yuan, W. et al. Increased atmospheric vapor pressure deficit reduces global vegetation growth. *Sci. Adv.* **5**, eaax1396 (2019).
- Zhang, Q. et al. The hysteretic evapotranspiration–vapor pressure deficit relation. *J. Geophys. Res.-Biogeosci.* **119**, 125–140 (2014).
- Berg, A. & Sheffield, J. Climate change and drought: the soil moisture perspective. *Curr. Clim. Change Rep.* **4**, 180–191 (2018).
- Donat, M. G. et al. More extreme precipitation in the world's dry and wet regions. *Nat. Clim. Change* **6**, 508–513 (2016).
- Asadieh, B. & Krakauer, N. Y. Global trends in extreme precipitation: climate models versus observations. *Hydrol. Earth Syst. Sc.* **19**, 877–891 (2015).
- Rajah, K. et al. Changes to the temporal distribution of daily precipitation. *Geophys. Res. Lett.* **41**, 8887–8894 (2014).
- McCabe, G. J. & Wolock, D. M. Long-term variability in Northern Hemisphere snow cover and associations with warmer winters. *Clim. Change* **99**, 141–153 (2010).
- Pulliaainen, J. et al. Patterns and trends of Northern Hemisphere snow mass from 1980 to 2018. *Nature* **581**, 294–298 (2020).
- Chai, Y. et al. Constrained Earth system models show a stronger reduction in future Northern Hemisphere snowmelt water. *Nat. Clim. Change* **15**, 514–520 (2025).
- Deng, Y. et al. Variation trend of global soil moisture and its cause analysis. *Ecol. Indic.* **110**, 105939 (2020).
- Zhang, Q. et al. A new high-resolution multi-drought-index dataset for mainland China. *Earth Syst. Sci. Data* **17**, 837–853 (2025).
- Zhao, M. & Running, S. W. Drought-induced reduction in global terrestrial net primary production from 2000 through 2009. *Science* **329**, 940–943 (2010).
- Xu, C. et al. Increasing impacts of extreme droughts on vegetation productivity under climate change. *Nat. Clim. Chang* **9**, 948–953 (2019).
- Li, W. et al. Widespread and complex drought effects on vegetation physiology inferred from space. *Nat. Commun.* **14**, 4640 (2023).
- Pendergrass, A. G. et al. Flash droughts present a new challenge for subseasonal-to-seasonal prediction. *Nat. Clim. Chang* **10**, 191–199 (2020).
- Yuan, X. et al. A global transition to flash droughts under climate change. *Science* **380**, 187–191 (2023).
- Otkin, J. A. et al. Flash droughts: a review and assessment of the challenges imposed by rapid-onset droughts in the United States. *B Am. Meteorol. Soc.* **99**, 911–919 (2018).
- Christian, J. I. et al. A methodology for flash drought identification: Application of flash drought frequency across the United States. *J. Hydrometeorol.* **20**, 833–846 (2019).
- Christian, J. I. et al. Global distribution, trends, and drivers of flash drought occurrence. *Nat. Commun.* **12**, 6330 (2021).
- Mo, K. C. & Lettenmaier, D. P. Precipitation deficit flash droughts over the United States. *J. Hydrometeorol.* **17**, 1169–1184 (2016).
- Chai, Y. et al. Underestimating global land greening: future vegetation changes and their impacts on terrestrial water loss. *One Earth* **8**, 2101176 (2025).
- Zheng, H. et al. The impacts of erosion on the carbon cycle. *Rev. Geophys.* **63**, e2023RG000829 (2025).
- Chai, Y. et al. Global reduction in sensitivity of vegetation water use efficiency to increasing CO<sub>2</sub>. *J. Hydrol.* **641**, 131844 (2024).
- Crausbay, S. D. et al. Defining ecological drought for the twenty-first century. *B Am. Meteorol. Soc.* **98**, 2543–2550 (2017).
- Zhang, B. et al. A water-energy balance approach for multi-category drought assessment across globally diverse hydrological basins. *Agr. Meteorol.* **264**, 247–265 (2019).
- Vicente-Serrano, S. M. et al. Response of vegetation to drought time-scales across global land biomes. *Proc. Natl. Acad. Sci. USA* **110**, 52–57 (2013).
- Zhang, Y., Keenan, T. F. & Zhou, S. Exacerbated drought impacts on global ecosystems due to structural overshoot. *Nat. Ecol. Evol.* **5**, 1490–1498 (2021).
- Yu, Z. et al. Global gross primary productivity and water use efficiency changes under drought stress. *Environ. Res. Lett.* **12**, 014016 (2017).
- Batllori, E. et al. Forest and woodland replacement patterns following drought-related mortality. *Proc. Natl. Acad. Sci. USA* **117**, 29720–29729 (2020).
- DeSoto, L. et al. Low growth resilience to drought is related to future mortality risk in trees. *Nat. Commun.* **11**, 545 (2020).
- Yang, Y. et al. Studying drought-induced forest mortality using high spatiotemporal resolution evapotranspiration data from thermal satellite imaging. *Remote Sens Environ.* **265**, 112640 (2021).

33. Cox, P. M., Betts, R. A. & Collins, M. Amazonian forest dieback under climate-carbon cycle projections for the 21st century. *Theor. Appl. Clim.* **78**, 137–156 (2004).
34. Huntingford, C., Zelazowski, P. & Galbraith, D. Simulated resilience of tropical rainforests to CO<sub>2</sub>-induced climate change. *Nat. Geosci.* **6**, 268–273 (2013).
35. Zuidema, P. A. et al. Tropical tree growth driven by dry-season climate variability. *Nat. Geosci.* **15**, 269–276 (2022).
36. McDowell, N. G. et al. Mechanisms of woody-plant mortality under rising drought, CO<sub>2</sub> and vapour pressure deficit. *Nat. Rev. Earth Environ.* **3**, 294–308 (2022).
37. Sippel, S. et al. Drought, heat, and the carbon cycle: a review. *Curr. Clim. Change Rep.* **4**, 266–286 (2018).
38. Senf, C. et al. Excess forest mortality is consistently linked to drought across Europe. *Nat. Commun.* **11**, 6200 (2020).
39. Choat, B. et al. Global convergence in the vulnerability of forests to drought. *Nature* **491**, 752–755 (2012).
40. Sevanto, S. Drought impacts on phloem transport. *Curr. Opin. Plant Biol.* **43**, 76–81 (2018).
41. Carnicer, J. et al. Widespread crown condition decline, food web disruption, and amplified tree mortality with increased climate change-type drought. *Proc. Natl. Acad. Sci. USA* **108**, 1474–1478 (2011).
42. Van Mantgem, P. J. et al. Widespread increase of tree mortality rates in the western United States. *Science* **323**, 521–524 (2009).
43. Phillips, O. L. et al. Drought–mortality relationships for tropical forests. *N. Phytol.* **187**, 631–646 (2010).
44. Breshears, D. D. et al. Regional vegetation die-off in response to global-change-type drought. *Proc. Natl. Acad. Sci. USA* **102**, 15144–15148 (2005).
45. Allen, C. D. et al. A global overview of drought and heat-induced tree mortality reveals emerging climate change risks for forests. *Ecol. Manag.* **259**, 660–684 (2010).
46. Worrall, J. J. et al. Recent declines of *Populus tremuloides* in North America linked to climat. *Ecol. Manag.* **299**, 35–51 (2013).
47. Allen, C. D., Breshears, D. D. & McDowell, N. G. On underestimation of global vulnerability to tree mortality and forest die-off from hotter drought in the Anthropocene. *Ecosphere* **6**, 1–55 (2015).
48. Stocker, B. D. et al. Drought impacts on terrestrial primary production underestimated by satellite monitoring. *Nat. Geosci.* **12**, 264–270 (2019).
49. Wu, C. et al. An evaluation framework for quantifying vegetation loss and recovery in response to meteorological drought based on SPEI and NDVI. *Sci. Total Environ.* **906**, 167632 (2024).
50. Li, Y. et al. Widespread spring phenology effects on drought recovery of Northern Hemisphere ecosystems. *Nat. Clim. Chang* **13**, 182–188 (2023).
51. Fathi-Taperasht, A. et al. Influence of drought duration and severity on drought recovery period for different land cover types: evaluation using MODIS-based indices. *Ecol. Indic.* **141**, 109146 (2022).
52. Mackie, K. A. et al. Plant functional groups mediate drought resistance and recovery in a multisite grassland experiment. *J. Ecol.* **107**, 937–949 (2019).
53. Barbeta, A. et al. The combined effects of a long-term experimental drought and an extreme drought on the use of plant-water sources in a Mediterranean forest. *Glob. Change Biol.* **21**, 1213–1225 (2015).
54. Zhang, M. & Yuan, X. Rapid reduction in ecosystem productivity caused by flash droughts based on decade-long FLUXNET observations. *Hydrol. Earth Syst. Sc.* **24**, 5579–5593 (2020).
55. Otkin, J. A. et al. Assessing the evolution of soil moisture and vegetation conditions during a flash drought–flash recovery sequence over the South-Central United States. *J. Hydrometeorol.* **20**, 549–562 (2019).
56. Otkin, J. A. et al. Assessing the evolution of soil moisture and vegetation conditions during the 2012 United States flash drought. *Agric. Meteorol.* **218**, 230–242 (2016).
57. He, M. et al. Impacts of the 2017 flash drought in the US Northern plains informed by satellite-based evapotranspiration and solar-induced fluorescence. *Environ. Res. Lett.* **14**, 074019 (2019).
58. Hersbach, H. et al. The ERA5 global reanalysis. *Q. J. R. Meteor. Soc.* **146**, 1999–2049 (2020).
59. Yuan, X. et al. Anthropogenic shift towards higher risk of flash drought over China. *Nat. Commun.* **10**, 4661 (2019).
60. Wang, L. & Yuan, X. Two types of flash drought and their connections with seasonal drought. *Adv. Atmos. Sci.* **35**, 1478–1490 (2018).
61. Ma, F. & Yuan, X. The propagation from atmospheric flash drought to soil flash drought and its changes in a warmer climate. *J. Hydrol.* **654**, 132877 (2025).
62. Wang, D. et al. Drought resistance of vegetation and its change characteristics before and after the implementation of the Grain for Green Program on the Loess Plateau, China. *Remote Sens.-Basel* **14**, 5142 (2022).
63. Wu, X. et al. Differentiating drought legacy effects on vegetation growth over the temperate Northern Hemisphere. *Glob. Change Biol.* **24**, 504–516 (2018).
64. Anderegg, W. R. et al. Pervasive drought legacies in forest ecosystems and their implications for carbon cycle models. *Science* **349**, 528–532 (2015).
65. Markewitz, D. et al. Soil moisture depletion under simulated drought in the Amazon: impacts on deep root uptake. *N. Phytol.* **187**, 592–607 (2010).
66. Mattos, C. R. et al. Double stress of waterlogging and drought drives forest–savanna coexistence. *Proc. Natl. Acad. Sci. USA* **120**, e2301255120 (2023).
67. Fan, Y., Li, H. & Miguez-Macho, G. Global patterns of groundwater table depth. *Science* **339**, 940–943 (2013).
68. Jiang, L. et al. Assessing vegetation resilience and vulnerability to drought events in Central Asia. *J. Hydrol.* **634**, 131012 (2024).
69. Liu, L. et al. Revisiting assessments of ecosystem drought recovery. *Environ. Res. Lett.* **14**, 114028 (2019).
70. Vermote, E. et al. *NOAA Climate Data Record (CDR) of Normalized Difference Vegetation Index (NDVI), Version 4* (NOAA’s National Climatic Data Center: Asheville, NC, USA, 2014).
71. Cowling, R. M. et al. Rainfall reliability, a neglected factor in explaining convergence and divergence of plant traits in fire-prone Mediterranean-climate ecosystems. *Glob. Ecol. Biogeogr.* **14**, 509–519 (2005).
72. Coppola, E. et al. Climate hazard indices projections based on CORDEX-CORE, CMIP5 and CMIP6 ensemble. *Clim. Dynam.* **57**, 1293–1383 (2021).
73. Defourny, P. et al. Land Cover Climate Change Initiative—Product User Guide v2. Issue 2.0. *ESA-UCLouvain-Geomatics, Louvain-la-Neuve, Belgium, Tech. Rep* (2017).
74. Fernández-Martínez, M. et al. Global trends in carbon sinks and their relationships with CO<sub>2</sub> and temperature. *Nat. Clim. Change* **9**, 73–79 (2019).
75. Wang, S. et al. Recent global decline of CO<sub>2</sub> fertilization effects on vegetation photosynthesis. *Science* **370**, 1295–1300 (2020).
76. Chai, Y. et al. Homogenization and polarization of the seasonal water discharge of global rivers in response to climatic and anthropogenic effects. *Sci. Total Environ.* **709**, 136062 (2020).
77. Rohde, R. A. & Hausfather, Z. The Berkeley Earth land/ocean temperature record. *Earth Syst. Sci. Data* **12**, 3469–3479 (2020).
78. Harris, I. et al. Version 4 of the CRU TS monthly high-resolution gridded multivariate climate dataset. *Sci. Data* **7**, 109 (2020).
79. Plummer, S., Lecomte, P. & Doherty, M. The ESA Climate Change Initiative (CCI): A European contribution to the generation of the

- Global Climate Observing System. *Remote Sens Environ.* **203**, 2–8 (2017).
80. Boschetti, L. et al. Global validation of the Collection 6 MODIS burned area product. *Remote Sens Environ.* **235**, 111490 (2019).
81. Chuvieco, E., Pettinari, M. L., Otón, G. ESA Fire Climate Change Initiative (Fire\_cci): AVHRR-LTDR Burned Area Pixel product, version 1.1. *Centre for Environmental Data Analysis*, 21 December (2020).

## Acknowledgements

Y.C. acknowledges support from the National Natural Science Foundation of China (42301018). C.M. acknowledges support from the National Natural Science Foundation of China (U24A20572). J.P. was supported by the Catalan Government grants SGR 2021–1333 and AGAUR2023 CLIMA 00118.

## Author contributions

Y.C. and C.M. led the writing, designed the research and performed the data analysis. A.A., Y.P., Y.F., X.L., J.J., Q.Z., and J.P. discussed the design, methods and results and helped writing and revising the manuscript.

## Competing interests

The authors declare no competing interests.

## Additional information

**Supplementary information** The online version contains supplementary material available at <https://doi.org/10.1038/s41467-025-67173-x>.

**Correspondence** and requests for materials should be addressed to Chiyuan Miao.

**Peer review information** *Nature Communications* thanks Jeffrey Basara, Benjamin Bright and the other, anonymous, reviewer(s) for their contribution to the peer review of this work. A peer review file is available.

**Reprints and permissions information** is available at <http://www.nature.com/reprints>

**Publisher's note** Springer Nature remains neutral with regard to jurisdictional claims in published maps and institutional affiliations.

**Open Access** This article is licensed under a Creative Commons Attribution-NonCommercial-NoDerivatives 4.0 International License, which permits any non-commercial use, sharing, distribution and reproduction in any medium or format, as long as you give appropriate credit to the original author(s) and the source, provide a link to the Creative Commons licence, and indicate if you modified the licensed material. You do not have permission under this licence to share adapted material derived from this article or parts of it. The images or other third party material in this article are included in the article's Creative Commons licence, unless indicated otherwise in a credit line to the material. If material is not included in the article's Creative Commons licence and your intended use is not permitted by statutory regulation or exceeds the permitted use, you will need to obtain permission directly from the copyright holder. To view a copy of this licence, visit <http://creativecommons.org/licenses/by-nc-nd/4.0/>.

© The Author(s) 2025